RoDyGS: Robust Dynamic Gaussian Splatting for Casual Videos

Yoonwoo Jeong*
POSTECH
jeongyw12382@postech.ac.kr

Junmyeong Lee*
POSTECH
jmlee24@postech.ac.kr

Hoseung Choi*
POSTECH
sseung45@postech.ac.kr

Minsu Cho
POSTECH
mscho@postech.ac.kr

Abstract

*Dynamic view synthesis (DVS) has advanced remarkably in recent years, achieving high-fidelity rendering while reducing computational costs. Despite the progress, optimizing dynamic neural fields from casual videos remains challenging, as these videos do not provide direct 3D information, such as camera trajectories or the underlying scene geometry. In this work, we present **RoDyGS**, an optimization pipeline for dynamic Gaussian Splatting from casual videos. It effectively learns motion and underlying geometry of scenes by separating dynamic and static primitives, and ensures that the learned motion and geometry are physically plausible by incorporating motion and geometric regularization terms. We also introduce a comprehensive benchmark, **Kubric-MRig**, that provides extensive camera and object motion along with simultaneous multi-view captures, features that are absent in previous benchmarks. Experimental results demonstrate that the proposed method significantly outperforms previous pose-free dynamic neural fields and achieves competitive rendering quality compared to existing pose-free static neural fields. The code and data are publicly available at https://rodygs.github.io/.*

1. Introduction

We live in a dynamic world where objects with complex geometry and textures undergo intricate motion and deformation. Casual videos are typically used to capture these movement in everyday scenarios. However, casual videos provide only 2D projections and lack essential 3D information, such as camera trajectories and the detailed geometry and motion of scenes. Recent advancements in computer graphics have explored effective methods for reconstructing 3D scene structures and motion from visual data, in-
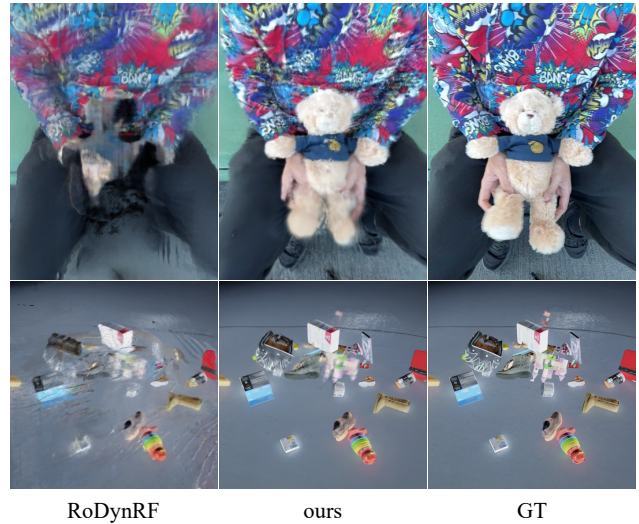

Figure 1. **Robust Dynamic Gaussian Splatting (RoDyGS).** RoDyGS achieves high-fidelity rendering of novel viewpoints from casual videos, significantly outperforming RoDynRF, which struggles with blurriness during substantial camera and object movement.

cluding casual videos. Building on the success of Neural Radiance Fields (NeRF) [38] for static scenes, subsequent research [41–43] has extended NeRF to dynamic view synthesis (DVS) by incorporating time-dependent deformation fields.

In static scenes, existing neural fields typically rely on COLMAP [49] to estimate camera parameters from a set of observations. However, the estimation often fails under challenging conditions, such as large camera pose changes or dynamic scenes. Recent approaches [9] leverage pose priors [32, 54] trained on large-scale 3D datasets to achieve more effective and robust reconstructions. Nonetheless, these methods assume that all objects remain stationary during video capture, which limits their applicability to casual

---

* denotes the equal contribution.

videos.

Recently, RoDynRF [35] has aimed to address dynamic scenes by jointly estimating camera parameters and dynamic neural fields. While it demonstrates promising results for specific forward-facing scenes, its optimization strategy—relying on randomly initialized camera parameters-easily falls into local minima, limiting its effectiveness in real-world scenarios.

In this work, we propose **RoDyGS**, which fully leverages geometric priors from MASt3R [32], a geometric foundation model for multi-view stereo, to render casually captured videos. RoDyGS decomposes the static and dynamic parts of scenes using motion masks generated by the Track Anything Model (TAM) [60]. Next, we initialize static and dynamic Gaussians with depth information acquired during pose initialization. Additionally, we introduce regularization terms inspired by object geometry and motion optimization perspectives to accurately reconstruct scene geometry and object motion.

Furthermore, we illustrate that previous benchmarks face challenges in evaluating both pose estimation and rendering quality due to the absence of ground truth (GT) camera poses or the lack of concurrent multi-view captures. Therefore, we introduce a challenging benchmark, **Kubric-MRig**, which includes photorealistic scenes with a variety of simultaneously captured viewpoints with extensive camera and object movement. Our experiments show that RoDyGS outperforms previous pose-free dynamic neural fields on Kubric-MRig and iPhone [15], and shows competitive rendering quality with pose-free static neural fields on Tanks and Temples [27].

In summary, our contributions are as follows:

1. We introduce a pose-free optimization pipeline, RoDyGS, which separates the static and dynamic components of scenes to render casual videos.
2. RoDyGS introduces regularization terms to ensure that learned motion and geometry are physically plausible.
3. We present Kubric-MRig, a challenging dataset designed to evaluate both pose estimation and rendering quality in dynamic scenes, addressing limitations found in previous benchmarks.
4. Our experiments demonstrate that RoDyGS surpasses previous pose-free dynamic neural fields on Kubric-MRig and iPhone [15] datasets, while also achieving competitive rendering quality with pose-free static neural fields on the Tanks and Temples [27] benchmark.

2. Related work

2.1. Novel View Synthesis on Static Scenes

Novel View Synthesis (NVS) is a task of generating novel viewpoints from a set of observations. Pioneering work in NVS leverages point clouds [28, 59, 68], meshes [46, 47],

and planes [19] for geometrically convincing view synthesis. Recently, NeRF [39] has achieved ground-breaking rendering quality by representing volumetric scene functions via MLPs. To accelerate the training and inference of NeRF, subsequent research focuses on baking trained NeRFs [18] or directly optimizing explicit representations [11, 40, 50].

More recently, 3D Gaussian Splatting (3DGS) [24] has introduced a novel rendering algorithm that rasterizes anisotropic 3D Gaussians into image planes. Its efficient tile-based alpha-blending CUDA implementation offers real-time rendering without quality degradation, achieving state-of-the-art results on NVS benchmarks. Subsequent work based on 3DGS has proposed methods to improve fidelity [25, 64], enable training with sparse views [58, 67], and facilitate editing [5, 7]. Despite their advancements, these approaches assume all objects remain stationary when scene captures and that camera poses are fully available, restricting their practical application.

2.2. Novel View Synthesis on Dynamic Scenes

Following the success of NVS in stationary scenes, researchers have extended neural fields to capture both the underlying motion and geometry of scenes from a set of observations. The pioneer work [41–43] learns additional time-varying deformation fields built on top of NeRF. Several studies [4, 12, 33] have taken a different approach by focusing on learning multi-dimensional feature fields. These methods encode scene dynamics without relying on explicit motion representations. With the emergence of 3DGS, [36, 57] propose learning the trajectories of individual Gaussians over time. Subsequent research has introduced more efficient representations, such as factorized motion bases [29] and sparse control points [20]. Another line of work by [63] extends spherical harmonics into a 4D spherindrical harmonics function, integrating both time-dependent and view-dependent components.

As highlighted by Dycheck [15], many existing approaches focus on unrealistic scenarios, such as camera teleportation or scenes with ambient motion, whereas multi-view capture is typically performed with casual videos that involve substantial motion. However, reconstructing dynamic scenes from these videos is a highly ill-posed problem, often failing without additional cues due to the ambiguity between camera and object movement. To resolve this problem, recent efforts [31, 35, 52, 55] leverage pretrained depth estimation models [44, 61] or long-term trajectory tracking models [23]. In this work, we also utilize off-the-shelf models, MASt3R [32] and DepthAnything [61], as effective guidance to achieve accurate optimization results.

2.3. Pose-free Static and Dynamic Neural Fields

Traditional NVS pipelines strongly rely on structure from motion (SfM) [49] to obtain camera poses from a set of ob-

servations. There has been growing interests in optimizing neural fields without pre-calibrated camera poses since SfM processes are often time-intensive and vulnerable to deformation and motion of dynamic objects. The pioneer work iNeRF [65] estimates camera poses from pre-trained NeRF by minimizing discrepancy between query and rendered views. [2, 6, 21, 34, 56] optimize both camera and NeRF parameters using photometric loss and geometric regularization. After the emergence of 3DGS, CF-3DGS [13] proposes progressively growing 3DGS for pose estimation. InstantSplat [9] utilizes DUSt3R [54] for initializing poses and point clouds in 3DGS. While effective on stationary scenes, these models are not suitable for real-world casual videos that involve complex motion and deformation.

Recently, RoDynRF [35] introduces a pose-free optimization method for dynamic neural fields from casual videos by separating static backgrounds from dynamic objects. However, this approach is limited to forward-facing scenes or scenes with small viewpoint changes. To overcome these limitations, we use the geometric foundation model MASt3R, enabling our method to handle a wider range of video capture scenarios. Additionally, by leveraging the explicit structure of 3DGS, our optimization pipeline includes geometric regularization to improve rendering quality.

Our concurrent work [53] shares similar inspiration with ours. Specifically, motion masks can be effortlessly obtained from video inputs using the Track Anything Model (TAM) [60], requiring just a few user interactions. By leveraging these motion masks and casually captured videos, both [53] and RoDyGS enable realistic rendering. While [53] relies on external motion-related cues, RoDyGS achieves robust motion learning without such dependencies. Our pipeline explicitly separate static and dynamic components and optimize Gaussians with carefully designed regularization objectives.

3. Method

In this section, we present RoDyGS, an optimization pipeline for dynamic Gaussian Splatting from casual videos. We begin with a brief overview of 3D Gaussian Splatting (3DGS) [24] and the motion representation introduced by DynMF [29] in Section 3.1. Following this, we detail our overall optimization process in Section 3.2. In the subsequent sections, we introduce regularization terms to ensure consistent geometry in Section 3.3 and to capture complex motion in Section 3.4. Finally, we elaborate the details of training RoDyGS in Section 3.5.

3.1. Preliminary: Dynamic 3D Gaussian Splatting

Static Representation. 3DGS represents scene geometry using Gaussian primitives and achieves real-time and high-fidelity rendering through an efficient tile-based ras-

terization. Specifically, each 3D Gaussian is defined by a mean vector $\boldsymbol{\mu}_c$ and a 3D covariance matrix $\boldsymbol{\Sigma}_c$. Then the Gaussians are splatted onto the image plane by approximating [69] their 2D means and covariances as follows:

$$\boldsymbol{\mu}_c^{2D} = \boldsymbol{\Pi}(KE\boldsymbol{\mu}_c), \quad \boldsymbol{\Sigma}_c^{2D} = \boldsymbol{J}\boldsymbol{E}\boldsymbol{\Sigma}_c\boldsymbol{E}^T\boldsymbol{J}^T, \quad (1)$$

where $\boldsymbol{J}$ denotes the Jacobian of the affine approximation of the projective transformation, and $\boldsymbol{K}$ and $\boldsymbol{E}$ denote intrinsic and extrinsic matrix of camera, respectively. $\boldsymbol{\Pi}$ denotes perspective projection of 3D points into an image plane. Each covariance matrix is decomposed into a rotation matrix $\boldsymbol{R}_c$ and a scaling matrix $\boldsymbol{S}_c$ such that $\boldsymbol{\Sigma}_c = \boldsymbol{R}_c\boldsymbol{S}_c\boldsymbol{S}_c^T\boldsymbol{R}_c^T$. In addition, each Gaussian includes opacity $\alpha \in \mathbb{R}$ and spherical harmonics (SH) coefficients $\boldsymbol{c} \in \mathbb{R}^{(L+1)^2}$ to represent view-dependent color. Thus, the final color of a pixel $\boldsymbol{x}_p$ is computed as:

$$C_p = \sum_{i=1}^{N} c_i\alpha_i T_i \mathcal{N}\left(\boldsymbol{x}_p|\boldsymbol{\mu}_c^{2D}, \boldsymbol{\Sigma}_c^{2D}\right), \quad (2)$$

where $T_i = \prod_{j=1}^{i-1}\left(1 - \alpha_j\mathcal{N}\left(\boldsymbol{x}_p|\boldsymbol{\mu}_c^{2D}, \boldsymbol{\Sigma}_c^{2D}\right)\right)$, and c_i and α_i represent the color and opacity associated with each 3D Gaussian, respectively.

Dynamic Representation. DynMF [29] extends 3DGS to handle dynamic scenes by modeling the trajectory of each Gaussian through learnable motion bases. It defines B shared motion bases that predict translation($\boldsymbol{b}^\mu$) and rotation($\boldsymbol{b}^q$) as unit quaternion vectors. Each Gaussian has motion coefficients $\boldsymbol{m}$ with a dimension of B, time-varying pose of Gaussian is represented by combination of these motion coefficients and the shared motion bases. With a motion bases function ϕ, DynMF predicts time-dependent motion of each Gaussian for timestep t as follows:

$$(\boldsymbol{b}^\mu(t), \boldsymbol{b}^q(t)) = \phi(\frac{t}{T}), \quad (3)$$

where ϕ is learnable motion estimation network, that receives the normalized timestep in the range $[0, 1]$ by dividing the timestep t with the maximum timestep T. We use a set of shallow MLP networks to optimize motion representation. Then the time-dependent motion parameter $\boldsymbol{\mu}(t)$ and $\boldsymbol{q}(t)$ are obtained as follows:

$$\boldsymbol{\mu}(t) = \boldsymbol{\mu}_c + \boldsymbol{m} \cdot \boldsymbol{b}^\mu(t), \quad \boldsymbol{q}(t) = \boldsymbol{q}_c + \boldsymbol{m} \cdot \boldsymbol{b}^q(t). \quad (4)$$

Note that $\boldsymbol{q}(t)$ are quaternion representations and can be converted into time-dependent rotation matrices, $\boldsymbol{R}(t)$. The rest of rendering process follows the original 3DGS with $\mathbf{R}(t)$, and mean vectors, $\boldsymbol{\mu}(t)$.
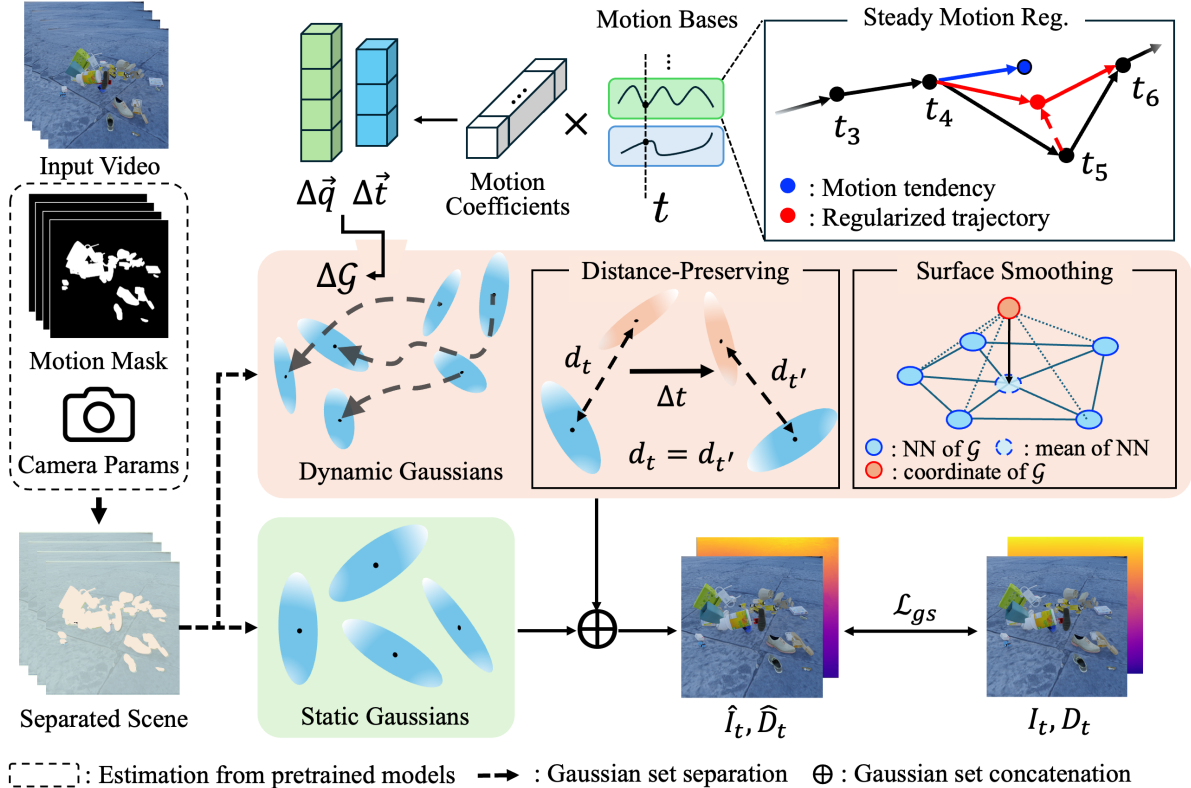
Figure 2. **RoDyGS Pipeline Overview.** Starting with a casually captured video input, RoDyGS extracts camera poses and depths using MASt3R [32], while motion masks are derived from TAM [60]. It then separates static and dynamic Gaussians, enabling each to be independently learned for stationary background and moving objects. The primary optimization objective, L_{gs}, includes photometric loss and Pearson depth loss, with depth guidance extracted from images using DepthAnything [61]. Additionally, for dynamic Gaussians, Gaussian distance-preserving regularization ($\mathcal{L}_{tc}$) and surface smoothness regularization ($\mathcal{L}_s$) are applied. For the motion bases, continuous motion regularization ($\mathcal{L}_{mc}$) is employed.

3.2. Overall Pipeline

RoDyGS processes a sequence of T video frames, $\{I_t \in \mathbb{R}^{H \times W \times 3}\}_{t=1}^{T}$, capturing a dynamic scene. It optimizes Gaussian attributes, motion bases, and camera poses to accurately render novel views for a given query viewpoint and timestep. We visualize the overall pipeline in Figure 2.

Joint Optimization. Dynamic scenes, characterized by moving objects, often pose challenges for traditional Structure from Motion (SfM) techniques, which may struggle to accurately estimate camera poses. To address these inaccuracies, we propose a joint optimization of scene geometry and camera poses. Specifically, we begin by estimating initial camera poses and geometry from the provided image sequence using MASt3R [32]. Subsequently, we perform a joint optimization of the camera poses and Gaussian features.

Static-Dynamic Scene Separation. We model the dynamic scene as a combination of a static background and dynamic objects. In detail, we partition the dynamic Gaussian field into two distinct sets: a set of static Gaussians, $\mathcal{G}_S$, which represents the background, and a set of dynamic Gaussians, $\mathcal{G}_D$, which represents the moving objects. For clear separation between static and dynamic parts, we employ dynamic object masks derived from a pretrained video tracking model, Track Anything Model (TAM) [60].

As noted in RoDynRF [35], the separation of dynamic and static representations enhances the robustness of the optimization process. This approach mitigates ambiguities between camera and object movement during joint optimization by associating camera motion with static geometry. Furthermore, this separation permits the application of specific regularization terms; for instance, motion regularization should be exclusively applied to the dynamic components. The various regularization terms employed in this method will be elaborated upon in the subsequent sections.

3.3. Object Geometry Regularization

As discussed in the previous section, the task of dynamic view synthesis (DVS) from casual videos is inherently challenging due to insufficient information about moving objects and occluded regions throughout the video sequences. In many frames, the visible portions of a moving object's body are often limited, making it difficult to observe their complete geometry. Additionally, parts or even entire objects are frequently obscured by obstacles, such as static elements in the environment or other moving objects. It is important that the geometry of objects remain consistent across different timesteps and allow for smooth reconstruction. To ensure these properties, we propose two regularization terms for the dynamic Gaussians, $\mathcal{G}_D$.

Distance-Preserving Across Time. For a Gaussian g and its neighbors $NN(g)$, we introduce a distance-preserving regularization to ensure temporal consistency. We define the regularization term for a Gaussian g as follows:

$$d(g_1, g_2, t) = \|\boldsymbol{\mu}_{g_1}(t) - \boldsymbol{\mu}_{g_2}(t)\|_2^2, \quad g_1, g_2 \in \mathcal{G}, \quad (5)$$

$$l_{tc}(g, t) = \frac{1}{K|\mathcal{T}'|} \sum_{\substack{g' \in NN(g) \\ t' \in \mathcal{T}'}} \|d(g, g', t) - d(g, g', t')\|_2^2, \quad (6)$$

where $\boldsymbol{\mu}_g(t)$ is the mean vector of Gaussian g at time t, and $\mathcal{T}'$ is a set of sampled timesteps.

Object Surface Smoothing. We apply an object surface smoothing regularization to mitigate perturbations in the local geometry of objects. The motion of individual Gaussians may not accurately preserve local geometry, occasionally resulting in inconsistent object surfaces over time. To address this issue, we employ a geometric regularization similar to prior work [26] in mesh reconstruction, aimed at reducing these inconsistencies. For the closest K neighbors of a Gaussian g, we enforce the Gaussian's location to be close to the mean of its neighbors, defined as follows:

$$l_s(g, t) = \|\boldsymbol{\mu}_g(t) - \frac{1}{K} \sum_{g' \in NN(g)} \boldsymbol{\mu}_{g'}(t)\|_2^2. \quad (7)$$

During training, we apply both objectives, a distance-preserving objective $\mathcal{L}_{tc}$ and a surface regularization objective $\mathcal{L}_s$, to a randomly sampled Gaussian set $\mathcal{G}' \subset \mathcal{G}_D$ at time t as follows:

$$\mathcal{L}_{tc} = \frac{1}{|\mathcal{G}'|} \sum_{g \in \mathcal{G}'} l_{tc}(g, t), \quad \mathcal{L}_s = \frac{1}{|\mathcal{G}'|} \sum_{g \in \mathcal{G}'} l_s(g, t), \quad (8)$$

$$\mathcal{L}_{og} = \lambda_{tc}\mathcal{L}_{tc} + \lambda_s\mathcal{L}_s, \quad (9)$$

where λ_{tc} and λ_s are balancing parameters for each regularization term.

3.4. Motion Regularization

Prior research [1, 29, 30] has shown that the complex motion of objects can often be approximated as low-rank 3D motion. In our work, this low-rank motion bias is implicitly captured through a learnable motion basis representation using bottlenecked MLPs [17, 48]. To explicitly incorporate this bias and mitigate perturbations in the trajectory bases, we introduce motion continuity regularization, which directly constrains the learned motion trajectories predicted from the motion bases.

Steady Motion Assumption. To effectively learn motion bases that represent real-world dynamics, we assume that motion remains consistent and does not exhibit drift over short time intervals. Based on this assumption of steady motion, we apply regularization to the motion bases as follows:

$$l_{mc,i}(t) = \|\phi_i(\frac{t}{T}) - \phi_i(\frac{t-1}{T})\|_2^2, \quad (10)$$

where $\phi_i \in \boldsymbol{\phi}$ is the i-th motion basis. Note that this motion regularization is equivalent to a simplified momentum-preserving equation in kinematics, assuming a fixed particle mass, which effectively maintains steady motion over time.

Weighted Motion Regularization. While our steady motion assumption is sufficient to model most real-world motions, it may not capture complex or fine-grained details in some cases. To prevent over-smoothing during motion optimization, we apply weighted motion regularization to each motion basis. Our explicit regularization scheme allows us to easily adjust the complexity of the motion bases. To apply varying levels of steady motion regularization, we determine the weight for regularization using a weight generation function. The modified form of the regularization is as follows:

$$\mathcal{L}_{mc} = \frac{1}{B(T-1)} \sum_{t=2}^{T} \sum_{i=1}^{B} w_i l_{mc,i}(t). \quad (11)$$

The regularization weight w_i adjusts the strength of regularization and varies based on the value of a cumulative exponential function as i changes.

3.5. Optimization

As described in previous section, RoDyGS jointly optimizes gaussian features, motion basis, and camera poses with various regularization terms.

Loss Function. We use photometric losses as in the original 3DGS optimization pipeline. Specifically, we apply an

L_1 reconstruction loss and an SSIM loss between the rendered and target images:

$$\mathcal{L}_{\text{recon}} = \lambda_{l1}(\|\hat{I}_t - I_t\|_1) + \lambda_{\text{SSIM}}(\frac{1 - \text{SSIM}(\hat{I}_t, I_t)}{2}). \quad (12)$$

Additionally, we incorporate scene geometry information using monocular depth maps obtained from DepthAnything [61]. However, due to the scale ambiguity of the predicted monocular depths, we cannot directly compare these predictions with the rendered scene depth from the Gaussians. To address this issue, we apply the Pearson depth loss $\mathcal{L}_{\text{depth}}$ [58], which maximize the linear correlation between the rendered depth and the estimated depth. Specifically, $\mathcal{L}_{\text{depth}}$ is designed to maximize the linear correlation between the rendered depth map $\hat{D}_t$ and the estimated depth D_t, as follows:

$$\mathcal{L}_{\text{depth}} = \frac{1}{N} \sum_{t=1}^{N_F} \left(1 - \mathcal{E}(\hat{D}_t, D_t)\right), \quad (13)$$

$$\mathcal{E}(\hat{D}_t, D_t) = \frac{\mathbb{E}[\hat{D}_t D_t] - \mathbb{E}[\hat{D}_t]\mathbb{E}[D_t]}{\sigma[\hat{D}_t] \cdot \sigma[D_t]}, \quad (14)$$

where σ is the standard deviation. We compute global depth loss $\mathcal{L}_{\text{depth},g}$ to match global depth maps and local depth loss $\mathcal{L}_{\text{depth},l}$ to compare local statistics, which remove local noise of depth, as follows:

$$\mathcal{L}_{\text{depth}} = \lambda_{\text{depth},g}\mathcal{L}_{\text{depth},g} + \lambda_{\text{depth},l}\mathcal{L}_{\text{depth},l}. \quad (15)$$

Thus, our final loss is as follows:

$$\mathcal{L} = \mathcal{L}_{gs} + \mathcal{L}_{og} + \mathcal{L}_{\text{depth}} + \mathcal{L}_{mc}. \quad (16)$$

Implementation Details. Our problem is highly ill-posed, so we use various data-driven priors to resolve ambiguities during optimization. To address these ambiguity issues, we employ pretrained priors to estimate initialization parameters and depth maps. Specifically, we use MASt3R [32] to initialize the camera poses and point clouds for 3D Gaussian Splatting. Additionally, we estimate monocular depth maps using DepthAnything [61]. Further training details are provided in the supplementary material.

4. Experiments

4.1. Dataset: Kubric-MRig

We revisit previous benchmarks – Sintel [3], Tanks and Temples [27], D-NeRF [43], NVIDIA dynamic [66], HyperNeRF [42], and iPhone [15] – on Dynamic View Synthesis(DVS) to assess the suitability for pose estimation and view synthesis performance. As summarized in Table 1, the previous benchmarks have several limitations: they offer restricted viewpoints such as forward-facing

Dataset	Wide Viewpoints	Large Motion	GT CAM	Backgrounds
Sintel [3]	✗	✓	✓	✓
T & T [27]	✓	✗	✗	✓
D-NeRF [43]	✓	✓	✓	✗
NVIDIA [66]	✗	✓	✓	✓
HyperNeRF [42]	✗	✓	✗	✓
iPhone [15]	✗	✓	✓	✓
Kubric-MRig (ours)	✓	✓	✓	✓

Table 1. **Benchmarks for DVS.** Previous benchmarks either lack wide viewpoints, large motion, ground truth cameras, or backgrounds, whereas Kubric-MRig satisfies all these criteria.

scenes [3, 15, 42, 66], feature no motion [27], lack ground truth camera poses [27, 66], and miss backgrounds [43]. To address these limitations, we introduce Kubric-Mrig, a dataset specifically designed to evaluate both pose estimation and NVS performance for dynamic scenes with large movement of cameras and objects and also includes accurate ground truth camera poses.

To construct the Kubric-MRig dataset, we employ Kubric [16], a Blender-based synthetic scene generator. Each scene consists of a 100-frame monocular video captured by moving a camera around the objects for training purposes. Following the evaluation protocol of [66], the test camera is fixed at the initial position of the training video, while the timestep varies across the 100 viewpoints used for training. Further details are provided in the Appendix.

4.2. Dynamic View Synthesis for Casual Videos

Evaluation on Kubric-MRig. We compare RoDyGS with previous dynamic neural fields that are trained with [35, 43, 57, 62, 63] and without [62] ground truth camera poses. Following the evaluation protocol of [66], we assess the DVS quality with PSNR, SSIM, and LPIPS, and the pose estimation quality with ATE, RPE-R, and RPE-t. We found that the dynamic mask generated by RoDynRF, which utilizes RAFT flow and MaskRCNN, fails to produce reliable motion masks. For a fair comparison with RoDyGS, we additionally train RoDynRF [35] with dynamic mask given by Track Anything Model (TAM) [60].

As reported in Table 2 and Table 3, RoDyGS notably outperforms RoDynRF for both DVS and pose estimation quality. As visualized in Figure 3, RoDynRF struggles with blurry rendering of objects and scene backgrounds, while RoDyGS produces clear images. Additionally, RoDyGS preserves the shapes of dynamic objects, whereas RoDynRF fails to do so, with parts of objects partially disappearing. Note that the entire training and rendering process of RoDyGS takes around 2 hours with a single RTX 3090 GPU, while RoDynRF takes around 2 days. Furthermore, RoDyGS renders objects with quality that is better than or comparable to [35, 43, 57, 57, 62], which use ground truth camera poses for training.

6

Kubric-MRig	CAM	PSNR(↑)	SSIM(↑)	LPIPS(↓)		iPhone	CAM	PSNR(↑)	SSIM(↑)	LPIPS(↓)
D-NeRF [43]	✓	20.65	0.7160	0.4021		D-NeRF [43]	✓	22.04	0.5820	0.4952
RoDynRF [35]	✓	20.80	0.7584	0.4836		RoDynRF [35]	✓	16.78	0.5096	0.4943
4DGS1 [57]	✓	22.46	0.8557	0.1760		4DGS1 [57]	✓	21.25	0.5865	0.4142
Deform3D [62]	✓	22.66	0.8478	0.1877		Deform3D [62]	✓	22.81	0.6950	0.3094
4DGS2 [63]	✓	23.02	0.8460	0.1898		4DGS2 [63]	✓	25.52	0.7843	0.2535
RoDynRF [35]	✗	18.36	0.6121	0.5984		RoDynRF [35]	✗	14.91	0.4050	0.5531
RoDynRF [35] + TAM [60]	✗	16.93	0.6157	0.6224		RoDynRF [35] + TAM [60]	✗	13.87	0.3670	0.5900
ours	✗	**19.44**	**0.7169**	**0.3401**		ours	✗	**17.38**	**0.4656**	**0.4361**

Table 2. **DVS quality on Kubric-MRig(left) and iPhone(right).** CAM denotes the availability of ground truth camera poses during training. RoDyGS achieves superiority over RoDynRF for novel view rendering quality.

	ATE(↓)	RPE-R(↓)	RPE-t(↓)
RoDynRF [35]	0.0632	1.8255	0.4088
RoDynRF [35] + TAM [60]	0.0695	1.8746	0.4701
ours	**0.0052**	**0.0933**	**0.0374**

Table 3. **Pose estimation performance on Kubric-MRig.** RoDyGS achieves significantly better pose estimation quality than RoDynRF. We have excluded COLMAP for comparison since 3 scenes fail over 8 scenes.

	PSNR(↑)	SSIM(↑)	LPIPS(↓)	ATE(↓)	RPE-R(↓)	RPE-t(↓)
NeRFmm [56]	22.50	0.59	0.54	0.123	0.477	1.735
SC-NeRF [21]	23.76	0.65	0.48	0.129	0.489	1.890
BARF [34]	23.42	0.61	0.54	0.078	0.441	1.046
Nope-NeRF [2]	26.34	0.74	0.39	0.006	**0.038**	0.080
CF-3DGS [13]	31.28	**0.93**	0.09	**0.004**	0.069	**0.041**
ours	**31.51**	**0.93**	**0.08**	0.007	0.096	0.052

Table 4. **Comparison of pose-free NVS methods on Tanks and Temples.** Novel view rendering and pose estimation performance on Tanks and Temples with pose-free static neural fields. RoDyGS achieves competitive performance with CF-3DGS.

Evaluation on iPhone. Similar to the experiments conducted on Kubric-MRig, we evaluate RoDyGS on a real-world casual video dataset, iPhone [15]. However, the existing evaluation protocol for the iPhone dataset is designed under the assumption of using ground truth cameras when training DVS models, as the training and test cameras are positioned far apart. Since RoDyGS and RoDynRF [35] do not use ground truth camera poses, we need an additional step to align the test camera to the correct position relative to the calibrated training cameras. This can lead to inaccurate evaluation if the test camera is misaligned. Therefore, we have reorganized the training and test split from a single camera to enable accurate alignment of test camera poses and re-evaluated the baseline models [35, 43, 57, 62, 63] accordingly. For more details about iPhone dataset, please refer to the Appendix.

As presented in Table 2 and Figure 3, RoDyGS significantly outperforms RoDynRF in both quantitative and qualitative evaluations. Specifically, RoDyGS accurately renders dynamic objects in their correct positions, whereas RoDynRF struggles to do so. Additionally, RoDyGS achieves a clearer separation between static backgrounds and dynamic objects, resulting in backgrounds that are rendered clearly, unlike those produced by RoDynRF.

4.3. Pose-Free Static Novel View Synthesis

As RoDyGS still works on static scenes, we compare RoDyGS with previous pose-free static neural fields [2, 13, 21, 34, 56] on Tanks and Temples [27]. For a fair comparison with previous baselines, we follow the same evaluation protocol with CF-3DGS [13]. As presented in Table 4, RoDyGS achieves rendering quality comparable to that of CF-3DGS. In terms of pose estimation quality, RoDyGS

performs slightly below CF-3DGS. Notably, CF-3DGS requires the training of hundreds of local Gaussians to optimize global Gaussians, resulting in considerable training time and memory consumption. Also note that Nope-NeRF [2] requires significantly more training and inference time than RoDyGS due to the high computational complexity of NeRF networks.

4.4. Ablation Studies

We conduct ablation studies on the regularization terms using the Kubric-MRig dataset. First, we train our model without any regularizations. Then, we incrementally add two regularizations, the object geometry regularization, $\mathcal{L}_{og}$, and the motion regularization, $\mathcal{L}_{mc}$. Table 5 demonstrates the effectiveness of our regularization terms. Notably, when $\mathcal{L}_{mc}$ is used, we have observed remarkable improvements.

In addition, we analyze the effectiveness of our steady motion regularization strategy. The term $\mathcal{L}_{mc,u}$ represents uniformly weighted motion regularization applied to all motion bases where all w_i are set to be the same across all Gaussians. Table 5 indicates that even with the uniform weighting, the steady motion regularization significantly enhances the rendering quality. We also compare RoDyGS with DynMF [29], which utilizes coefficient regularization, which is designed to enforce the spatial locality of motion.

As visualized in Figure 4, our regularization significantly enhances the rendering quality. Geometric regularization alone can lead to minor artifacts near object boundaries, such as the edges of the red basket. While uniformly weighted motion regularization helps sharpen these boundaries, it does not fully restore the fine geometric details of
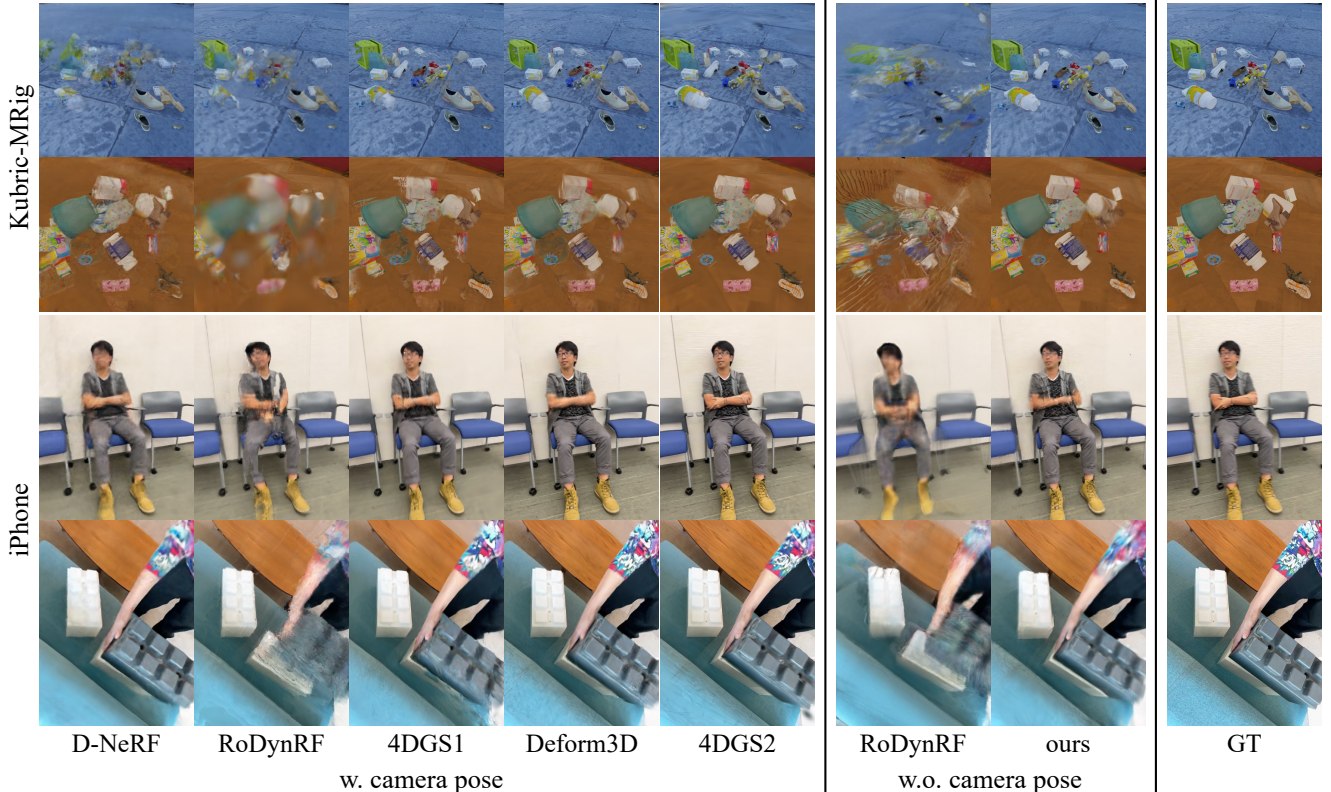
Figure 3. **Qualitative results on Kubric-MRig and iPhone.** Our pipeline accurately reconstructs scene geometry, produces sharp renderings, and aligns object positions well. Without GT camera poses, RoDynRF struggles to learn the scene geometry, resulting in object positions that differ from the GT. Even with GT camera poses, RoDynRF produces blurry results.

	PSNR(↑)	SSIM(↑)	LPIPS(↓)
DynMF [29]	18.92	0.7058	0.3513
no reg.	19.05	0.7063	0.3525
+ $\mathcal{L}_{og}$	19.08	0.7122	0.3481
+ $\mathcal{L}_{og}$ + $\mathcal{L}_{mc,u}$	19.43	**0.7184**	0.3406
+ $\mathcal{L}_{og}$ + $\mathcal{L}_{mc}$	**19.44**	0.7169	**0.3401**

Table 5. **Ablation studies.** We conduct ablation studies by varying regularization terms on Kubric-MRig. We have found that leveraging motion regularization shows remarkable improvement. We also compare RoDyGS with DynMF, which leverage motion coefficient regularization to ensure spatial consistency of learned motion.

the object. However, our weighted regularization technique better preserves object geometry, resulting in a perceptually higher-quality rendering although it contributes marginal gains from the uniform weighted regularization in quantitative performance.

5. Conclusion

In this work, we have introduced RoDyGS, a novel and robust optimization pipeline designed for dynamic Gaussian Splatting from casual videos. Unlike existing methods,
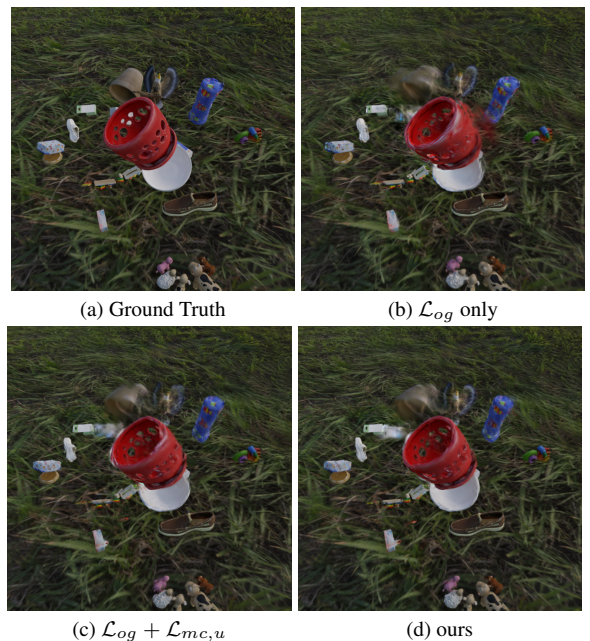

Figure 4. **Impact of regularization terms.** Our regularization effectively enhances the perceptual quality of the rendering results, leading to sharper and more realistic renderings.

RoDyGS achieves this by separating static and dynamic primitives, enabling it to effectively capture complex scene motion as well as the underlying geometry. RoDyGS proposes novel motion and geometric regularization terms, ensuring that the resulting scene properties are not only highly accurate but also physically plausible. To enable rigorous evaluation, we have introduced Kubric-MRig, a comprehensive benchmark specifically designed to challenge existing dynamic view synthesis methods. This benchmark captures extensive camera and object movement, as well as simultaneous multi-view sequences—characteristics that are critical for testing the limits of dynamic scene modeling. Our ablation studies demonstrate the effectiveness of the proposed regularization terms, ensuring the learning of physically plausible motion and geometry. Furthermore, experimental results reveal that RoDyGS outperforms prior pose-free dynamic neural fields and achieves rendering quality comparable to pose-free static neural fields.

RoDyGS: Robust Dynamic Gaussian Splatting for Casual Videos
Supplementary Materials

F. Dataset

F.1. Tanks and Temples

For evaluation on the Tanks and Temples dataset [27], we follow the same protocol as CF-3DGS [13]. In detail, we use 12.5% of the frames for evaluation, while the remaining frames are used for training. All remaining images are used for training.

Since pose-free models are trained without camera pose information, an additional alignment step is required for evaluation on novel viewpoints. During evaluation, we first align all test camera poses to the training camera poses before computing metrics. Specifically, we initialize each test camera pose by finding its nearest neighbor among the calibrated training camera poses, then refine it by minimizing the photometric error between the rendered and ground truth test images. To enable fair comparison between RoDyGS and static pose-free neural fields, we disable all motion detection by setting all motion masks to zero when evaluating on static scenes.

F.2. iPhone

The iPhone dataset [15] was originally designed for evaluating pose-aware novel view synthesis models. However, when evaluating pose-free models, we found that the large distances between test and training cameras made it difficult to accurately align test camera poses. To enable proper evaluation of pose-free neural fields, we modify the dataset split to follow CF-3DGS [13]'s protocol, which ensures test cameras remain close enough to training cameras for reliable pose alignment.

We evaluate on seven scenes from the iPhone dataset: *apple, block, paper-windmill, space-out, spin, teddy,* and *wheel*. For each scene, we use the first camera 0 (the training camera in the original dataset) to create our train/test split. Specifically, we use 12.5% of the frames for evaluation, while the remaining frames are used for training. This sampling strategy ensures that the test frames are well-distributed throughout the sequence while maintaining sufficient proximity to training frames. Following the evaluation protocol used in CF-3DGS, this proximity allows us to robustly align the test camera poses during evaluation.

F.3. Kubric-MRig

We elaborate the detail of the generation process of our Kubric-MRig dataset. Note that we implement our generation process referring to the Movi script, which is introduced in Kubric [16]. The main concern of our dataset is to avoid the potential ambiguity between camera and object motion, particularly when dynamic objects are excessively prominent than static ones. For instance, objects moving at the same velocity as the camera against a plain white background will appear stationary from the camera's perspective.

To construct each scene, we begin by selecting 15 to 35 objects from the Google Scanned Objects [8] dataset. We then place 10 to 20 of these objects on the ground plane, while positioning the remaining objects suspended in the air. To achieve natural-looking motion, we apply physics simulations to the dynamic objects, ensuring their movements closely resemble real-world dynamics. We point out that the objects on the ground plane exhibit dynamic motion due to collisions with each other, resulting in complex and realistic dynamics for each scene.

For training, we deploy 100 cameras that follow circular trajectories around the objects. Then, we follow the evaluation protocol proposed in [66] in our Kubric-MRig dataset to construct the evaluation setup. In detail, we fix the camera viewpoint to the first camera used during training and capture the scene across the 100 timesteps. All cameras are positioned equidistant from the world center, with distances randomly sampled between 15 and 20 units. To ensure comprehensive viewpoint coverage of the scenes for evaluation, we fix the elevation angle, which is randomly sampled from $30°$ to $60°$ during data capture. We provide a visualization of the generated dataset in Figure 6.

G. Implementation Details

G.1. Geometric Priors

Our optimization process begins with two initialization steps. First, we use MASt3R [32] to obtain initial scene geometry, running it with the 'swin' option, a window size of 10, and the iteration number of 200. Second, we use Track Anything Model (TAM) [60] to identify moving objects in the scene. Then, leveraging motion masks obtained from TAM, we separately initialize static and dynamic Gaussians. To initialize the point clouds for Gaussian Splatting (GS), we uniformly sample 120,000 points from the unprojected point clouds across all frames. For additional geometric supervision, we also employ monocular depths from DepthAnything [61]. For reproducibility, we use the official implementations and checkpoints.

G.2. Learnable Motion Basis

We employ a learnable motion basis representation implemented using a shallow MLP network, as proposed in DynMF [29]. The architecture consists of B learnable mo-

tion bases, structured as a shared time encoder and B motion prediction heads. In our experiments, we use the number of basis, B, of 16. The encoder is a 3-layer MLP, with input timestep expanded using sinusoidal embeddings at 26 frequency variations. It has a hidden layer with a width of 128 and uses the GELU activation function. Each motion prediction head is a 2-layer MLP with a width of 64, without activations in the final layer.

Additionally, we adopt Gaussian motion coefficient regularization from DynMF, incorporating the sparsity regularization losses $\mathcal{L}_m$ and $\mathcal{L}_{ms}$. Defining the motion coefficient vector $\boldsymbol{m}_i$ for the i-th Gaussian, these sparsity losses promote sparsity in the motion coefficient vector, thereby reducing overfitting and mitigating the impact of noisy motion in the training viewpoints. They are formally defined as:

$$\mathcal{L}_m = \frac{1}{NB} \sum_{i=1}^{N} \sum_{j=1}^{B} \|m_{ij}\|_1, \tag{17}$$

$$\mathcal{L}_{ms} = \frac{1}{N} \sum_{i=1}^{N} \left(\frac{1}{B} \sum_{j=1}^{B} \frac{\|m_{ij}\|_1}{\max_{1 \le k \le B} \|m_{ik}\|_1} \right). \tag{18}$$

Note that these motion sparsity losses are also applied to our optimization process.

For ablation studies, we reproduce DynMF by adding motion coefficient regularization instead of our proposed regularization terms.

This loss is defined for the motion coefficients of i-th and j-th Gaussians, $\boldsymbol{m}_i$ and $\boldsymbol{m}_j$, respectively:

$$\mathcal{L}_{\text{coeff}} = \frac{1}{Nk} \sum_{i=1}^{N} \sum_{j \in \text{NN}(\mathcal{G}_i)} \exp\left(-\lambda_w \|\boldsymbol{\mu}_i - \boldsymbol{\mu}_j\|_2^2\right) \|\boldsymbol{m}_i - \boldsymbol{m}_j\|_2^2. \tag{19}$$

This loss is applied to the k nearest neighbors of the i-th Gaussian, $\mathcal{G}_i$. Therefore, the total motion loss, originally proposed in DynMF is expressed as:

$$\mathcal{L}_{\text{motion}} = \lambda_{\text{coeff}} \mathcal{L}_{\text{coeff}} + \lambda_m \mathcal{L}_m + \lambda_{ms} \mathcal{L}_{ms}, \tag{20}$$

where λ_{coeff}, λ_m, and λ_{ms} are hyperparameters that control the contributions of each loss term.

G.3. Optimization

We use the official implementation of 3D Gaussian Splatting (3DGS), with modifications to enable gradient computation over camera poses. To avoid overfitting and stabilize the optimization process, we maintain the spherical harmonic (SH) coefficient degree of the Gaussians at 0. Afterward, we further optimize our model for 5000 steps, gradually increasing the SH coefficient degree every 1000 iterations, up to a maximum degree of 3. The weights assigned to each loss term during the optimization process are detailed in Table 6.

Loss Term	Weight
λ_{SSIM}	0.2
λ_{l1}	0.8
$\lambda_{\text{depth,g}}$	0.05
$\lambda_{\text{depth,l}}$	0.15
λ_{tc}	0.5
λ_s	0.5
λ_{mc}	0.1
λ_m	0.05
λ_{ms}	0.002

Table 6. Weights assigned to each loss term during the optimization process.

We use a linear warm-up strategy for learning rates during the first 10% of the total training steps, followed by cosine annealing for the rest of training steps. The peak learning rates are set to 1.0×10^{-5} for camera rotation and 1.0×10^{-6} for camera translation.

H. Discussion Regarding Motion Masks

H.1. Obtaining Motion Mask with Epipolar Errors

RoDynRF [35] uses motion masks derived from video frames to distinguish static and dynamic elements in scenes. To achieve this, RoDynRF leverages forward and backward optical flows of the video frames estimated by RAFT [51]. Then, it uses 8-point and RANSAC algorithm to estimate the fundamental matrix between adjacent frames. Afterward, it computes the error between the points projected using the fundamental matrix and those derived from the predicted flows. Regions with high error are assumed to correspond to dynamic parts of the frames. Although this approach produces reliable masks on previous benchmarks, we observed that this method often fails due to the large motion observed between adjacent frames in Kubric-MRig and iPhone dataset. Moreover, RoDynRF relies on hard-coded class names to generate clear masks, which involves failure for scenes with significant motion with non-hard-coded instances, thus limiting its practical applicability. RoDyGS instead leverages motion masks generated by the TAM [60], similar to those used in Shape of Motion [53]. We visualize generated masks in Figure 5.

H.2. Automatic Motion Masking using SAM

As mentioned in the previous section, RoDyGS employs TAM to extract motion masks for each frame in casual videos. Alternatively, we investigate the use of Segment Anything Model (SAM-v2) [45] to automatically mask dynamic objects with a text prompt. After testing various prompts, we found that the prompt '*objects*.' provided the best results.

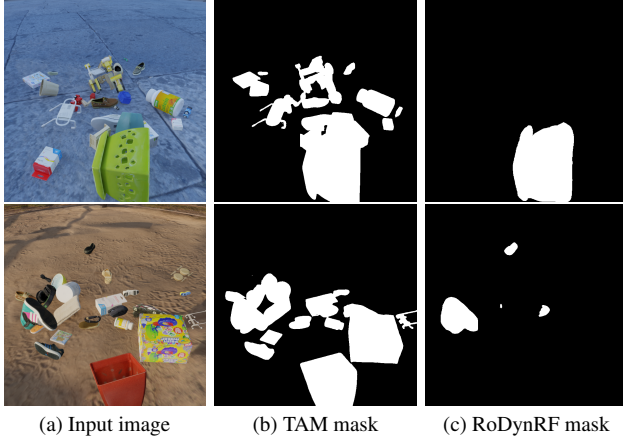|		
(a) Input image	(b) TAM mask	(c) RoDynRF mask

Figure 5. Comparison of motion masks between TAM [60] and RoDynRF [35].

Table 7 and Figure 12 compare RoDyGS with two variants: one using motion masks obtained by SAM and the other by TAM. Our findings indicate that there is no significant performance gap when using SAM. However, SAM is limited in its ability to extract motion masks in scenes with many stationary objects or dynamic backgrounds. Consequently, we opt to use TAM instead of SAM for improved quality, despite the minor manual efforts required.

I. Failure Cases and Future Work

I.1. Failure Cases

While RoDyGS demonstrates strong performance compared to RoDynRF [35], there are specific scenarios where failure cases can arise. One notable issue occurs when objects experience severe occlusion, making their geometry unobservable. In such cases, the reconstruction of the occluded object may be incomplete. As shown in the results of Kubric-MRig (upper rows of Figure 11), these limitations are evident, with the occluded parts of the object appearing collapsed. Nevertheless, RoDyGS preserves the appearance of observed parts by maintaining its time-consistent geometry.

Another failure case arises when objects exhibit large motions. In this scenario, the boundaries of the moving object can appear blurry during training, resulting in less sharp reconstructions. For instance, RoDynRF tends to overfit to specific timestep, failing to accurately model rapid object movement. Similar behaviors are also observed in our pipeline, indicating that large motion remains a significant challenge for such methods.

These cases highlight the need for further improvements to handle extreme object motion and occlusion effectively. Examples of these failure cases are visualized in Figure 11.

I.2. Limitations and Future Work

Dynamic Part Separation. To handle in-the-wild videos, we aim to develop a robust optimization pipeline leveraging off-the-shelf models. Our current procedure for separating dynamic and static parts relies on user interaction, making the pipeline partially manual. Segmenting dynamic parts in a video is a challenging task and remains an open topic in video processing. One future direction is to automate the separation of dynamic components during optimization. Our observations reveal that the static and dynamic parts were not clearly separated, leading to instability in the optimization process. A naive, automated dynamic part extraction process would be developed to mitigate this issue.

Camera Calibration. From camera calibration perspective, we intend to investigate advanced joint camera optimization techniques. Currently, our RoDyGS framework is heavily dependent on the initial camera parameters estimated MASt3R [32]. In cases where MASt3R provides inaccurate camera parameters, RoDyGS experiences diminished rendering quality. To alleviate this dependency, future research should focus on developing innovative methods that can robustly accommodate incorrectly calibrated camera poses. Furthermore, future studies should aim to estimate camera intrinsic parameters to enhance the accuracy of scene reconstruction.

Potential of 4DGS Representation. Our pipeline effectively converts 2D videos into 4D representations, making it valuable for a wide range of applications. Our 4D Gaussian representation captures 3D dynamics alongside the geometry of the scene, providing rich and detailed information that is challenging to infer directly from 2D perception alone. As pointed out by [22], unlike 2D perception, 3D-based perception directly represents real-world scene information, improving efficiency by eliminating the need for additional adaptors to convert 2D data into 3D representations. Further enhancing the informativeness of our 4D representation could significantly improve the accuracy and applicability of perception systems in various real-world scenarios.

J. Evaluation on NVIDIA Dynamic Dataset.

We evaluate RoDyGS against several baseline methods on the NVIDIA Dynamic dataset [66]. This dataset comprises 7 scenes, each captured with 12 fixed cameras arranged in a forward-facing configuration. Table 8 presents PSNR and LPIPS scores obtained from the NVIDIA Dynamic dataset. In Figure 9 visualizes the rendered results on the NVIDIA Dynamic dataset.

We experimentally observed that RoDynRF outperforms RoDyGS on the NVIDIA Dynamic dataset. We hypothesize that this phenomenon occurs because RoDynRF leverages

Kubric-MRig	PSNR(↑)	SSIM(↑)	LPIPS(↓)	iPhone	PSNR(↑)	SSIM(↑)	LPIPS(↓)
RoDynRF [35]	18.36	0.6121	0.5984	RoDynRF [35]	14.91	0.4050	0.5531
RoDynRF [35] + TAM [60]	16.93	0.6157	0.6224	RoDynRF [35] + TAM [60]	13.87	0.3670	0.5900
ours + SAM [45]	19.41	0.7152	0.3411	ours + SAM [45]	17.22	0.4606	0.4417
ours + TAM [60]	**19.44**	**0.7169**	**0.3401**	ours + TAM [60]	**17.38**	**0.4656**	**0.4361**

Table 7. **DVS quality comparison on Kubric-MRig (left) and iPhone (right) dataset.** We compare the performance among different motion mask extraction methods (SAM vs TAM) on both datasets.

PSNR (↑) / LPIPS (↓)	Jumping	Skating	Truck	Umbrella	Balloon1	Balloon2	Playground	Average
DynamicNeRF* [14]	24.68 / 0.090	**32.66** / **0.035**	28.56 / 0.082	23.26 / 0.137	22.36 / 0.104	**27.06** / **0.049**	24.15 / 0.080	**26.10** / 0.082
HyperNeRF [42]	18.34 / 0.302	21.97 / 0.183	20.61 / 0.205	18.59 / 0.443	13.96 / 0.530	16.57 / 0.411	13.17 / 0.495	17.60 / 0.367
TiNeuVox [10]	20.81 / 0.247	23.32 / 0.152	23.86 / 0.173	20.00 / 0.355	17.30 / 0.353	19.06 / 0.279	13.84 / 0.437	19.74 / 0.285
RoDynRF [35] w/ camera poses	**25.66** / **0.071**	28.68 / 0.040	**29.13** / **0.063**	**24.26** / **0.089**	**22.37** / **0.103**	26.19 / 0.054	**24.96** / **0.048**	25.89 / **0.065**
RoDynRF w/o camera poses	24.27 / 0.100	28.71 / 0.046	28.85 / 0.066	23.25 / 0.104	21.81 / 0.122	25.58 / 0.064	25.20 / 0.052	25.38 / 0.079
ours	22.86 / 0.214	26.30 / 0.089	26.58 / 0.134	22.93 / 0.170	20.94 / 0.224	25.22 / 0.128	23.30 / 0.095	24.02 / 0.151

Table 8. **Novel view synthesis results on NVIDIA Dynamic dataset.** Comparision of average PSNR and LPIPS evaluation results to existing methods on the NVIDIA Dynamic dataset [66].

normalized device coordinates [37], which assume that all scenes are captured in a forward-facing manner [66], providing a significant advantage over our method. Additionally, the dataset includes ambient camera motion and lacks temporal consistency across adjacent frames, making it less representative of real-world scenarios.

K. Scene-wise Qualitative Results

We visualize additional qualitative results of our work. Figure 7 visualizes rendered results of baselines and RoDyGS on Kubric-MRig. Then, Figure 8 presents the comparison between ours and pose-free 3D neural fields on Tanks and Temples. Finally, Figure 10 demonstrates our method's performance on the iPhone dataset compared to both pose-aware and pose-free approaches.

L. Scene-wise Quantitative Results

We report scene-wise scores to facilitate future research. Table 9, 10, 11, 12, 13, and 14 report scene-wise PSNR, SSIM, LPIPS, ATE, RPE-t, and RPE-R scores on Kubric-MRig, respectively. Then, Table 15, 16, and 17 report scene-wise PSNR, SSIM, and LPIPS scores on the iPhone [15] dataset, respectively.
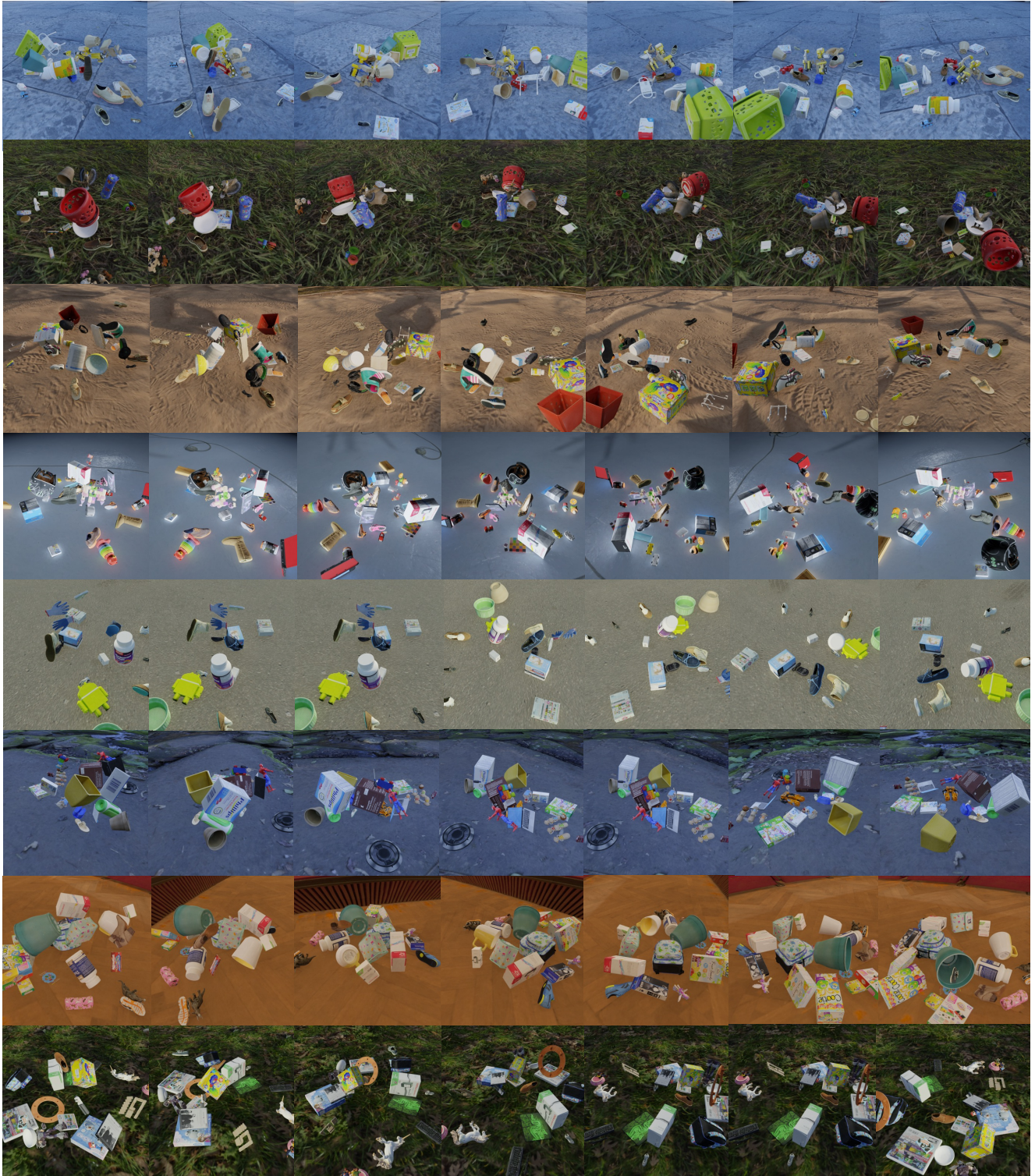
Figure 6. **Samples from Kubric-MRig.** Kubric-MRig is a dataset generated using Blender that contains 8 scenes. Each scene features multiple objects, some static and some in motion.
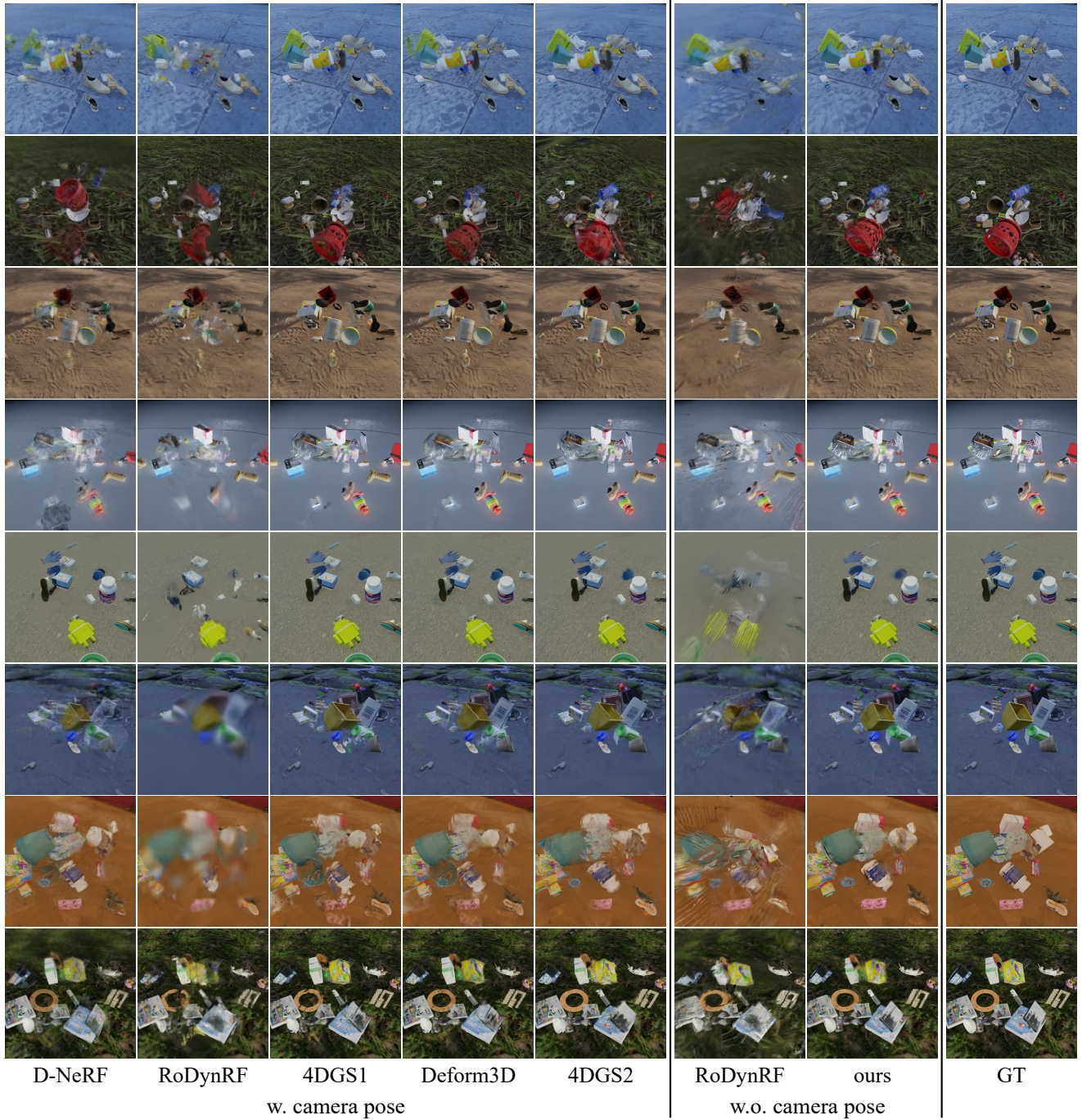
Figure 7. **Novel View Synthesis on Kubric-MRig.** Comparison of rendering results between RoDyGS and other dynamic neural field methods, both pose-aware [35, 43, 57, 62, 63] and pose-free [35]. In the pose-free setup, RoDyGS produces clearer rendering results than RoDynRF.
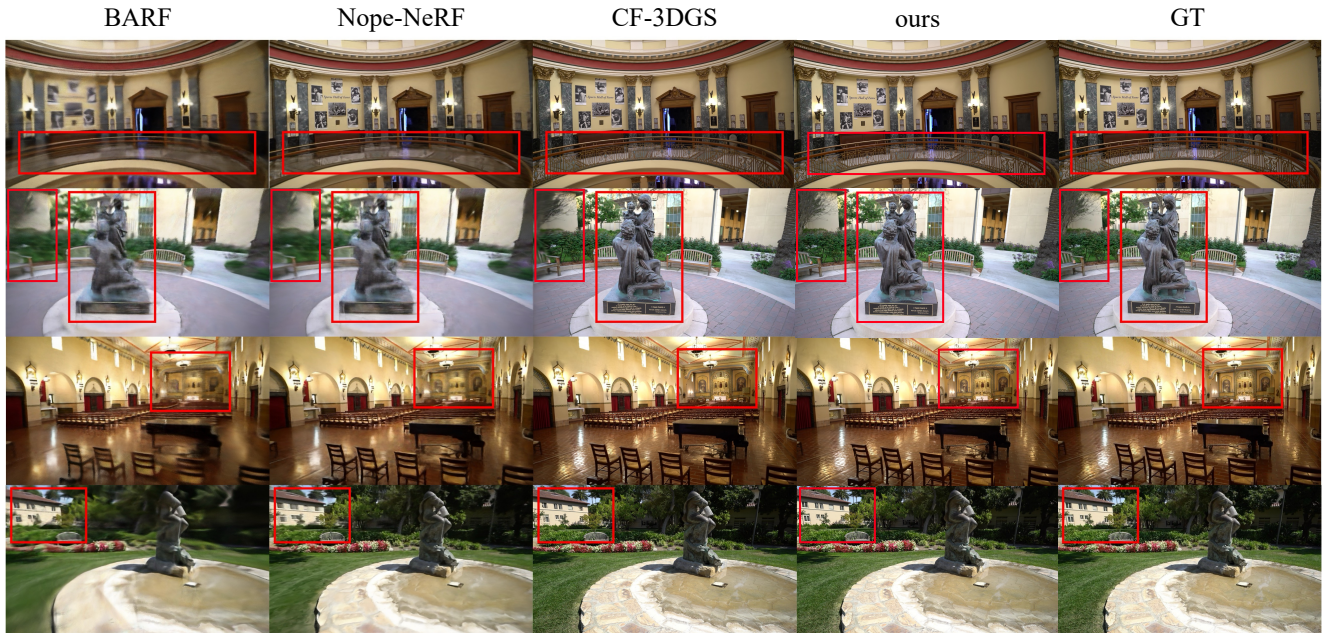
Figure 8. **Novel View Synthesis on Tanks and Temples.** Comparison on the Tanks and Temples dataset between RoDyGS and previous pose-free neural field methods [2, 13, 34]. RoDyGS demonstrates competitive rendering quality with CF-3DGS [13], the previous state-of-the-art pose-free neural field for static scenes.
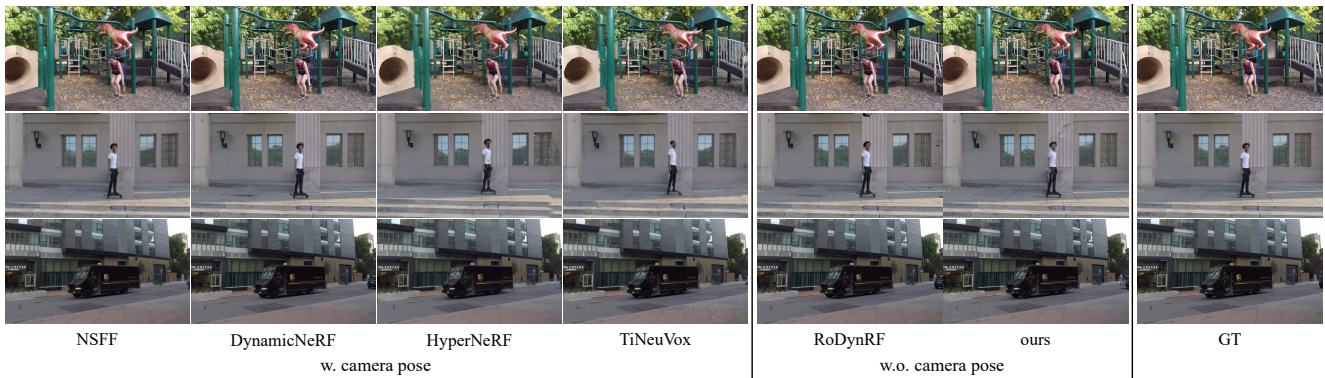
Figure 9. **Novel View Synthesis on NVIDIA Dynamic.** We compare RoDyGS with RoDynRF on NVIDIA Dynamic with the pose-free setup. RoDyGS synthesizes realistic images similar to those of RoDynRF.

D-NeRF	RoDynRF	4DGS1	Deform3D	4DGS2	RoDynRF	ours	GT
		w. camera pose			w.o. camera pose		

Figure 10. **Novel View Synthesis on iPhone.** We compare our RoDyGS method against both pose-aware [35, 43, 57, 62, 63] and pose-free [35] dynamic neural fields. RoDyGS achieves better visual clarity than RoDynRF under the pose-free setup.

D-NeRF	RoDynRF	4DGS1	Deform3D	4DGS2	RoDynRF	ours	GT
		w. camera pose			w.o. camera pose		

Figure 11. **Failure cases of RoDyGS.** RoDyGs and other baselines struggle from large motions and occlusion in scenes.

Figure 12. **Comparison of RoDyGS when leveraging SAM [45] and TAM [60] on Kubric-MRig.** RoDyGS with motion masks obtained by SAM achieves competitive visual quality to RoDyGS with motions masks obtained by TAM.

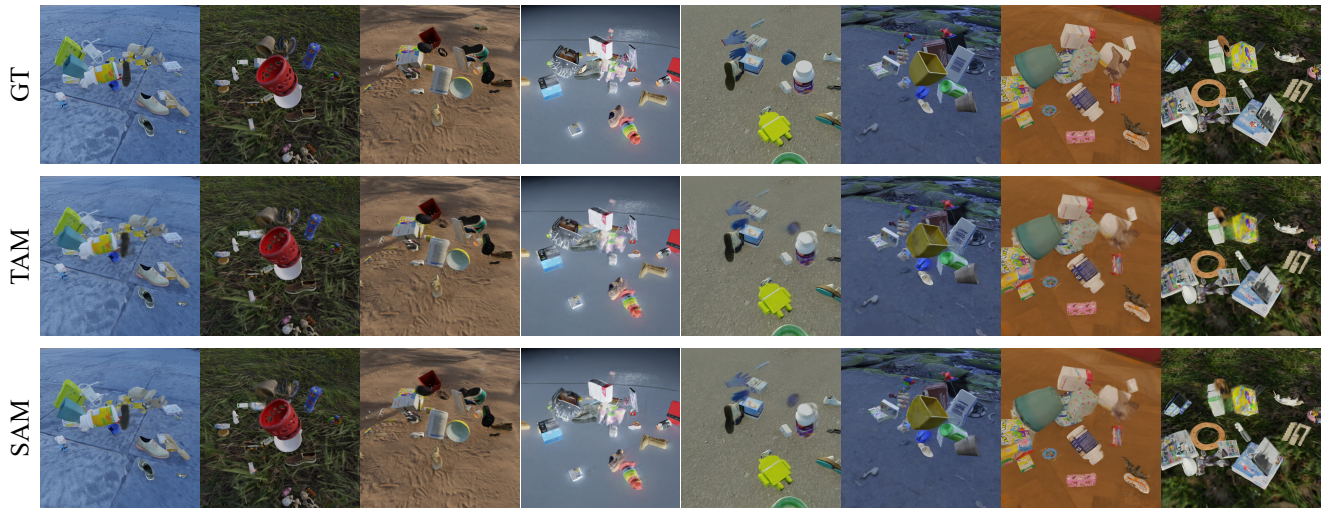| PSNR(↑)	scene0	scene1	scene2	scene3	scene4	scene5	scene6	scene7	average
D-NeRF [43]	21.95	19.90	22.73	20.56	23.62	20.61	19.11	16.68	20.65
RoDynRF [35]	23.19	21.44	22.82	20.56	22.39	20.74	18.00	17.30	20.80
4DGS1 [57]	24.68	23.38	24.95	21.76	23.92	22.65	20.19	18.13	22.46
Deform3D [62]	24.31	23.57	25.51	22.12	24.15	22.44	20.68	18.50	22.66
4DGS2 [63]	25.29	24.03	24.86	21.99	23.99	23.00	22.07	18.89	23.02
RoDynRF (w.o. pose) [35]	20.14	18.88	18.73	17.16	20.65	19.18	17.53	14.62	18.36
RoDynRF [35] + TAM [60] (w.o. pose)	18.82	15.89	18.09	16.55	20.01	16.80	16.28	12.98	16.93
ours	22.31	21.10	20.17	18.59	21.19	20.44	18.61	13.11	19.44

Table 9. **PSNR results for Kubric-MRig**

SSIM(↑)	scene0	scene1	scene2	scene3	scene4	scene5	scene6	scene7	average
D-NeRF [43]	0.7359	0.5533	0.7468	0.8069	0.7942	0.7299	0.7409	0.6202	0.7160
RoDynRF [35]	0.7773	0.6935	0.7854	0.8361	0.7299	0.8146	0.7707	0.6594	0.7584
4DGS1 [57]	0.8967	0.8802	0.9035	0.8563	0.8913	0.8639	0.7614	0.7924	0.8557
Deform3D [62]	0.8178	0.8791	0.8998	0.8675	0.8857	0.8513	0.7803	0.8013	0.8478
4DGS2 [63]	0.8695	0.8623	0.8846	0.8467	0.8806	0.8528	0.7856	0.7861	0.8460
RoDynRF (w.o. pose) [35]	0.6255	0.4772	0.6295	0.7153	0.6728	0.6958	0.6379	0.4432	0.6121
RoDynRF [35] + TAM [60] (w.o. pose)	0.6245	0.4457	0.6332	0.7351	0.6965	0.6522	0.6994	0.4393	0.6157
ours	0.7549	0.7043	0.7383	0.7667	0.7596	0.7810	0.6943	0.5360	0.7169

Table 10. **SSIM results for Kubric-MRig**

LPIPS (↓)	scene0	scene1	scene2	scene3	scene4	scene5	scene6	scene7	average
D-NeRF [43]	0.4165	0.5112	0.3884	0.3357	0.3521	0.4543	0.3222	0.4364	0.4021
RoDynRF [35]	0.4443	0.4627	0.4244	0.4427	0.5494	0.5074	0.5936	0.4438	0.4836
4DGS1 [57]	0.1192	0.1279	0.1122	0.2054	0.1339	0.1935	0.3090	0.2073	0.1760
Deform3D [62]	0.2013	0.1301	0.1300	0.1989	0.1445	0.2000	0.2974	0.1990	0.1877
4DGS2 [63]	0.1563	0.1455	0.1407	0.2263	0.1457	0.2012	0.2860	0.2168	0.1898
RoDynRF (w.o. pose) [35]	0.5869	0.6555	0.5811	0.5357	0.5883	0.6062	0.6258	0.6081	0.5984
RoDynRF [35] + TAM [60] (w.o. pose)	0.6246	0.7292	0.6203	0.5343	0.5917	0.6120	0.6200	0.6472	0.6224
ours	0.2928	0.2818	0.3130	0.3413	0.2938	0.3149	0.4347	0.4481	0.3401

Table 11. **LPIPS results for Kubric-MRig**

ATE(↓)	scene0	scene1	scene2	scene3	scene4	scene5	scene6	scene7	average
RoDynRF [35]	0.0881	0.0468	0.0824	0.0724	0.0319	0.0603	0.0446	0.0793	0.0632
RoDynRF [35] + TAM [60] (w.o. pose)	0.0818	0.0693	0.0826	0.0764	0.0361	0.0801	0.0704	0.0593	0.0695
ours	0.0009	0.0025	0.0071	0.0061	0.0045	0.0088	0.0028	0.0085	0.0052

Table 12. **ATE results for Kubric-MRig**

RPE-t(↓)	scene0	scene1	scene2	scene3	scene4	scene5	scene6	scene7	average
RoDynRF [35]	0.5425	0.3475	0.5030	0.4713	0.2174	0.3328	0.3190	0.5368	0.4088
RoDynRF [35] + TAM [60] (w.o. pose)	0.7732	0.4195	0.4228	0.6579	0.2550	0.4593	0.4750	0.2982	0.4701
ours	0.0083	0.0207	0.0563	0.0512	0.0320	0.0479	0.0223	0.0601	0.0374

Table 13. **RPE-t results for Kubric-MRig**

RPE-R(↓)	scene0	scene1	scene2	scene3	scene4	scene5	scene6	scene7	average
RoDynRF [35]	1.9904	1.6781	2.1122	1.7471	1.5009	1.9715	1.7836	1.8201	1.8255
RoDynRF [35] + TAM [60] (w.o. pose)	2.2493	1.7614	2.4783	1.8486	1.5099	1.8526	1.8043	1.4920	1.8746
ours	0.0187	0.0739	0.1004	0.1170	0.0902	0.1494	0.1036	0.0933	0.0933

Table 14. **RPE-R results for Kubric-MRig**

PSNR(↑)	apple	block	paper-windmill	space-out	spin	teddy	wheel	average
D-NeRF [43]	24.23	21.80	21.85	25.18	22.15	19.46	19.65	22.04
RoDynRF [35]	17.38	15.99	20.71	20.62	16.66	13.28	12.78	16.78
4DGS1 [57]	23.24	22.05	21.03	24.81	22.99	18.89	17.72	21.25
Deform3D [62]	24.82	23.26	20.62	26.95	23.51	20.93	19.56	22.81
4DGS2 [63]	27.31	25.09	26.81	29.54	26.30	21.11	22.45	25.52
RoDynRF (w.o. pose) [35]	14.50	14.73	17.94	18.06	15.75	11.56	11.85	14.91
RoDynRF [35] + TAM [60] (w.o. pose)	12.99	14.17	16.18	16.84	13.80	11.35	11.77	13.87
ours	16.79	17.67	19.20	19.16	18.47	14.69	15.66	17.38

Table 15. **PSNR results for iPhone.**

SSIM(↑)	apple	block	paper-windmill	space-out	spin	teddy	wheel	average
D-NeRF [43]	0.6748	0.6238	0.5129	0.7018	0.5002	0.4940	0.5665	0.5820
RoDynRF [35]	0.5310	0.4858	0.5760	0.6844	0.5139	0.3806	0.3959	0.5096
4DGS1 [57]	0.6512	0.6654	0.5080	0.7385	0.5283	0.5562	0.5224	0.5865
Deform3D [62]	0.7394	0.7377	0.5557	0.8177	0.6528	0.6899	0.6721	0.6950
4DGS2 [63]	0.8247	0.7912	0.8271	0.8533	0.7546	0.6652	0.7738	0.7843
RoDynRF (w.o. pose) [35]	0.4255	0.4524	0.3810	0.5975	0.3621	0.3250	0.2914	0.4050
RoDynRF [35] + TAM [60] (w.o. pose)	0.3873	0.4504	0.2966	0.5500	0.2976	0.2879	0.3014	0.3673
ours	0.4347	0.5369	0.4627	0.5808	0.3921	0.4015	0.4502	0.4656

Table 16. **SSIM results for iPhone.**

LPIPS(↓)	apple	block	paper-windmill	space-out	spin	teddy	wheel	average
D-NeRF [43]	0.4625	0.4957	0.4472	0.4452	0.5528	0.5433	0.5194	0.4952
RoDynRF [35]	0.5069	0.5702	0.4006	0.4167	0.4581	0.5675	0.5405	0.4943
4DGS1 [57]	0.4042	0.4031	0.3966	0.3469	0.4729	0.4276	0.4379	0.4142
Deform3D [62]	0.3029	0.3069	0.3924	0.2420	0.3294	0.3033	0.2888	0.3094
4DGS2 [63]	0.2448	0.2729	0.1569	0.2183	0.2860	0.3788	0.2166	0.2535
RoDynRF (w.o. pose) [35]	0.6022	0.5918	0.4244	0.5347	0.4950	0.6120	0.6114	0.5531
RoDynRF [35] + TAM [60] (w.o. pose)	0.6410	0.6282	0.5024	0.5299	0.5793	0.6744	0.5729	0.5897
ours	0.4850	0.4748	0.3569	0.4086	0.4278	0.4790	0.4203	0.4361

Table 17. **LPIPS results for iPhone.**

References

[1] Ijaz Akhter, Yaser Sheikh, Sohaib Khan, and Takeo Kanade. Nonrigid structure from motion in trajectory space. *Advances in neural information processing systems*, 21, 2008. 5

[2] Wenjing Bian, Zirui Wang, Kejie Li, Jia-Wang Bian, and Victor Adrian Prisacariu. Nope-nerf: Optimising neural radiance field with no pose prior. In *Proceedings of the IEEE/CVF Conference on Computer Vision and Pattern Recognition*, pages 4160–4169, 2023. 3, 7, 16

[3] D. J. Butler, J. Wulff, G. B. Stanley, and M. J. Black. A naturalistic open source movie for optical flow evaluation. In *European Conf. on Computer Vision (ECCV)*, pages 611–625. Springer-Verlag, 2012. 6

[4] Ang Cao and Justin Johnson. Hexplane: A fast representation for dynamic scenes. In *Proceedings of the IEEE/CVF Conference on Computer Vision and Pattern Recognition*, pages 130–141, 2023. 2

[5] Yiwen Chen, Zilong Chen, Chi Zhang, Feng Wang, Xiaofeng Yang, Yikai Wang, Zhongang Cai, Lei Yang, Huaping Liu, and Guosheng Lin. Gaussianeditor: Swift and controllable 3d editing with gaussian splatting. In *Proceedings of the IEEE/CVF Conference on Computer Vision and Pattern Recognition*, pages 21476–21485, 2024. 2

[6] Shin-Fang Chng, Sameera Ramasinghe, Jamie Sherrah, and Simon Lucey. Gaussian activated neural radiance fields for high fidelity reconstruction and pose estimation. In *European Conference on Computer Vision*, pages 264–280. Springer, 2022. 3

[7] Bin Dou, Tianyu Zhang, Yongjia Ma, Zhaohui Wang, and Zejian Yuan. Cosseggaussians: Compact and swift scene segmenting 3d gaussians with dual feature fusion. *CoRR*, 2024. 2

[8] Laura Downs, Anthony Francis, Nate Koenig, Brandon Kinman, Ryan Hickman, Krista Reymann, Thomas B McHugh, and Vincent Vanhoucke. Google scanned objects: A high-quality dataset of 3d scanned household items. In *2022 International Conference on Robotics and Automation (ICRA)*, pages 2553–2560. IEEE, 2022. 10

[9] Zhiwen Fan, Wenyan Cong, Kairun Wen, Kevin Wang, Jian Zhang, Xinghao Ding, Danfei Xu, Boris Ivanovic, Marco Pavone, Georgios Pavlakos, et al. Instantsplat: Unbounded sparse-view pose-free gaussian splatting in 40 seconds. *arXiv preprint arXiv:2403.20309*, 2024. 1, 3

[10] Jiemin Fang, Taoran Yi, Xinggang Wang, Lingxi Xie, Xiaopeng Zhang, Wenyu Liu, Matthias Nießner, and Qi Tian. Fast dynamic radiance fields with time-aware neural voxels. In *SIGGRAPH Asia 2022 Conference Papers*, 2022. 13

[11] Sara Fridovich-Keil, Alex Yu, Matthew Tancik, Qinhong Chen, Benjamin Recht, and Angjoo Kanazawa. Plenoxels: Radiance fields without neural networks. In *Proceedings of the IEEE/CVF conference on computer vision and pattern recognition*, pages 5501–5510, 2022. 2

[12] Sara Fridovich-Keil, Giacomo Meanti, Frederik Rahbæk Warburg, Benjamin Recht, and Angjoo Kanazawa. K-planes: Explicit radiance fields in space, time, and appearance. In *CVPR*, 2023. 2

[13] Yang Fu, Sifei Liu, Amey Kulkarni, Jan Kautz, Alexei A. Efros, and Xiaolong Wang. Colmap-free 3d gaussian splatting. In *Proceedings of the IEEE/CVF Conference on Computer Vision and Pattern Recognition (CVPR)*, pages 20796–20805, 2024. 3, 7, 10, 16

[14] Chen Gao, Ayush Saraf, Johannes Kopf, and Jia-Bin Huang. Dynamic view synthesis from dynamic monocular video. In *Proceedings of the IEEE International Conference on Computer Vision*, 2021. 13

[15] Hang Gao, Ruilong Li, Shubham Tulsiani, Bryan Russell, and Angjoo Kanazawa. Monocular dynamic view synthesis: A reality check. *Advances in Neural Information Processing Systems*, 35:33768–33780, 2022. 2, 6, 7, 10, 13

[16] Klaus Greff, Francois Belletti, Lucas Beyer, Carl Doersch, Yilun Du, Daniel Duckworth, David J Fleet, Dan Gnanapragasam, Florian Golemo, Charles Herrmann, Thomas Kipf, Abhijit Kundu, Dmitry Lagun, Issam Laradji, Hsueh-Ti (Derek) Liu, Henning Meyer, Yishu Miao, Derek Nowrouzezahrai, Cengiz Oztireli, Etienne Pot, Noha Radwan, Daniel Rebain, Sara Sabour, Mehdi S. M. Sajjadi, Matan Sela, Vincent Sitzmann, Austin Stone, Deqing Sun, Suhani Vora, Ziyu Wang, Tianhao Wu, Kwang Moo Yi, Fangcheng Zhong, and Andrea Tagliasacchi. Kubric: a scalable dataset generator. 2022. 6, 10

[17] Reinhard Heckel and Mahdi Soltanolkotabi. Compressive sensing with un-trained neural networks: Gradient descent finds a smooth approximation. In *International Conference on Machine Learning*, pages 4149–4158. PMLR, 2020. 5

[18] Peter Hedman, Pratul P Srinivasan, Ben Mildenhall, Jonathan T Barron, and Paul Debevec. Baking neural radiance fields for real-time view synthesis. In *Proceedings of the IEEE/CVF international conference on computer vision*, pages 5875–5884, 2021. 2

[19] Derek Hoiem, Alexei A Efros, and Martial Hebert. Automatic photo pop-up. In *ACM SIGGRAPH 2005 Papers*, pages 577–584. 2005. 2

[20] Yi-Hua Huang, Yang-Tian Sun, Ziyi Yang, Xiaoyang Lyu, Yan-Pei Cao, and Xiaojuan Qi. Sc-gs: Sparse-controlled gaussian splatting for editable dynamic scenes. In *Proceedings of the IEEE/CVF Conference on Computer Vision and Pattern Recognition*, pages 4220–4230, 2024. 2

[21] Yoonwoo Jeong, Seokjun Ahn, Christopher Choy, Anima Anandkumar, Minsu Cho, and Jaesik Park. Self-calibrating neural radiance fields. In *Proceedings of the IEEE/CVF International Conference on Computer Vision*, pages 5846–5854, 2021. 3, 7

[22] Yoonwoo Jeong, Seungjoo Shin, Junha Lee, Chris Choy, Anima Anandkumar, Minsu Cho, and Jaesik Park. Perfception: Perception using radiance fields. *Advances in Neural Information Processing Systems*, 35:26105–26121, 2022. 12

[23] Nikita Karaev, Ignacio Rocco, Benjamin Graham, Natalia Neverova, Andrea Vedaldi, and Christian Rupprecht. Cotracker: It is better to track together. *arXiv preprint arXiv:2307.07635*, 2023. 2

[24] Bernhard Kerbl, Georgios Kopanas, Thomas Leimkühler, and George Drettakis. 3d gaussian splatting for real-time radiance field rendering. *ACM Trans. Graph.*, 42(4):139–1, 2023. 2, 3

[25] Shakiba Kheradmand, Daniel Rebain, Gopal Sharma, Wei-wei Sun, Jeff Tseng, Hossam Isack, Abhishek Kar, Andrea Tagliasacchi, and Kwang Moo Yi. 3d gaussian splatting as markov chain monte carlo. *arXiv preprint arXiv:2404.09591*, 2024. 2

[26] Hyomin Kim, Hyeonseo Nam, Jungeon Kim, Jaesik Park, and Seungyong Lee. Laplacianfusion: Detailed 3d clothed-human body reconstruction. *ACM Transactions on Graphics (TOG)*, 41(6):1–14, 2022. 5

[27] Arno Knapitsch, Jaesik Park, Qian-Yi Zhou, and Vladlen Koltun. Tanks and temples: Benchmarking large-scale scene reconstruction. *ACM Transactions on Graphics (ToG)*, 36 (4):1–13, 2017. 2, 6, 7, 10

[28] Georgios Kopanas, Julien Philip, Thomas Leimkühler, and George Drettakis. Point-based neural rendering with per-view optimization. In *Computer Graphics Forum*, pages 29–43. Wiley Online Library, 2021. 2

[29] Agelos Kratimenos, Jiahui Lei, and Kostas Daniilidis. Dynmf: Neural motion factorization for real-time dynamic view synthesis with 3d gaussian splatting. *arXiV*, 2023. 2, 3, 5, 7, 8, 10

[30] Suryansh Kumar, Yuchao Dai, and Hongdong Li. Multi-body non-rigid structure-from-motion. In *2016 Fourth International Conference on 3D Vision (3DV)*, pages 148–156. IEEE, 2016. 5

[31] Yao-Chih Lee, Zhoutong Zhang, Kevin Blackburn-Matzen, Simon Niklaus, Jianming Zhang, Jia-Bin Huang, and Feng Liu. Fast view synthesis of casual videos. *arXiv preprint arXiv:2312.02135*, 2023. 2

[32] Vincent Leroy, Yohann Cabon, and Jérôme Revaud. Grounding image matching in 3d with mast3r. *arXiv preprint arXiv:2406.09756*, 2024. 1, 2, 4, 6, 10, 12

[33] Tianye Li, Mira Slavcheva, Michael Zollhoefer, Simon Green, Christoph Lassner, Changil Kim, Tanner Schmidt, Steven Lovegrove, Michael Goesele, Richard Newcombe, et al. Neural 3d video synthesis from multi-view video. In *Proceedings of the IEEE/CVF Conference on Computer Vision and Pattern Recognition*, pages 5521–5531, 2022. 2

[34] Chen-Hsuan Lin, Wei-Chiu Ma, Antonio Torralba, and Simon Lucey. Barf: Bundle-adjusting neural radiance fields. In *Proceedings of the IEEE/CVF international conference on computer vision*, pages 5741–5751, 2021. 3, 7, 16

[35] Yu-Lun Liu, Chen Gao, Andreas Meuleman, Hung-Yu Tseng, Ayush Saraf, Changil Kim, Yung-Yu Chuang, Johannes Kopf, and Jia-Bin Huang. Robust dynamic radiance fields. In *Proceedings of the IEEE/CVF Conference on Computer Vision and Pattern Recognition*, pages 13–23, 2023. 2, 3, 4, 6, 7, 11, 12, 13, 15, 17, 20, 21

[36] Jonathon Luiten, Georgios Kopanas, Bastian Leibe, and Deva Ramanan. Dynamic 3d gaussians: Tracking by persistent dynamic view synthesis. In *3DV*, 2024. 2

[37] Ben Mildenhall, Pratul P. Srinivasan, Rodrigo Ortiz-Cayon, Nima Khademi Kalantari, Ravi Ramamoorthi, Ren Ng, and Abhishek Kar. Local light field fusion: Practical view synthesis with prescriptive sampling guidelines. *ACM Transactions on Graphics (TOG)*, 2019. 13

[38] Ben Mildenhall, Pratul P. Srinivasan, Matthew Tancik, Jonathan T. Barron, Ravi Ramamoorthi, and Ren Ng. Nerf: Representing scenes as neural radiance fields for view synthesis. In *ECCV*, 2020. 1

[39] Ben Mildenhall, Pratul P Srinivasan, Matthew Tancik, Jonathan T Barron, Ravi Ramamoorthi, and Ren Ng. Nerf: Representing scenes as neural radiance fields for view synthesis. *Communications of the ACM*, 65(1):99–106, 2021. 2

[40] Thomas Müller, Alex Evans, Christoph Schied, and Alexander Keller. Instant neural graphics primitives with a multiresolution hash encoding. *ACM transactions on graphics (TOG)*, 41(4):1–15, 2022. 2

[41] Keunhong Park, Utkarsh Sinha, Jonathan T Barron, Sofien Bouaziz, Dan B Goldman, Steven M Seitz, and Ricardo Martin-Brualla. Nerfies: Deformable neural radiance fields. In *Proceedings of the IEEE/CVF International Conference on Computer Vision*, pages 5865–5874, 2021. 1, 2

[42] Keunhong Park, Utkarsh Sinha, Peter Hedman, Jonathan T. Barron, Sofien Bouaziz, Dan B Goldman, Ricardo Martin-Brualla, and Steven M. Seitz. Hypernerf: A higher-dimensional representation for topologically varying neural radiance fields. *ACM Trans. Graph.*, 40(6), 2021. 6, 13

[43] Albert Pumarola, Enric Corona, Gerard Pons-Moll, and Francesc Moreno-Noguer. D-NeRF: Neural Radiance Fields for Dynamic Scenes. In *Proceedings of the IEEE/CVF Conference on Computer Vision and Pattern Recognition*, 2020. 1, 2, 6, 7, 15, 17, 20, 21

[44] René Ranftl, Katrin Lasinger, David Hafner, Konrad Schindler, and Vladlen Koltun. Towards robust monocular depth estimation: Mixing datasets for zero-shot cross-dataset transfer. *IEEE Transactions on Pattern Analysis and Machine Intelligence (TPAMI)*, 2020. 2

[45] Nikhila Ravi, Valentin Gabeur, Yuan-Ting Hu, Ronghang Hu, Chaitanya Ryali, Tengyu Ma, Haitham Khedr, Roman Rädle, Chloe Rolland, Laura Gustafson, et al. Sam 2: Segment anything in images and videos. *arXiv preprint arXiv:2408.00714*, 2024. 11, 13, 19

[46] Gernot Riegler and Vladlen Koltun. Free view synthesis. In *Computer Vision–ECCV 2020: 16th European Conference, Glasgow, UK, August 23–28, 2020, Proceedings, Part XIX 16*, pages 623–640. Springer, 2020. 2

[47] Gernot Riegler and Vladlen Koltun. Stable view synthesis. In *Proceedings of the IEEE/CVF Conference on Computer Vision and Pattern Recognition*, pages 12216–12225, 2021. 2

[48] Basri Ronen, David Jacobs, Yoni Kasten, and Shira Kritchman. The convergence rate of neural networks for learned functions of different frequencies. *Advances in Neural Information Processing Systems*, 32, 2019. 5

[49] Johannes L Schonberger and Jan-Michael Frahm. Structure-from-motion revisited. In *Proceedings of the IEEE conference on computer vision and pattern recognition*, pages 4104–4113, 2016. 1, 2

[50] Cheng Sun, Min Sun, and Hwann-Tzong Chen. Improved direct voxel grid optimization for radiance fields reconstruction. *arXiv preprint arXiv:2206.05085*, 2022. 2

[51] Zachary Teed and Jia Deng. Raft: Recurrent all-pairs field transforms for optical flow. In *Computer Vision–ECCV*

2020: 16th European Conference, Glasgow, UK, August 23–28, 2020, Proceedings, Part II 16, pages 402–419. Springer, 2020. 11

[52] Qianqian Wang, Vickie Ye, Hang Gao, Jake Austin, Zhengqi Li, and Angjoo Kanazawa. Shape of motion: 4d reconstruction from a single video. 2024. 2

[53] Qianqian Wang, Vickie Ye, Hang Gao, Jake Austin, Zhengqi Li, and Angjoo Kanazawa. Shape of motion: 4d reconstruction from a single video. *arXiv preprint arXiv:2407.13764*, 2024. 3, 11

[54] Shuzhe Wang, Vincent Leroy, Yohann Cabon, Boris Chidlovskii, and Jerome Revaud. Dust3r: Geometric 3d vision made easy. In *Proceedings of the IEEE/CVF Conference on Computer Vision and Pattern Recognition*, pages 20697–20709, 2024. 1, 3

[55] Shizun Wang, Xingyi Yang, Qiuhong Shen, Zhenxiang Jiang, and Xinchao Wang. Gflow: Recovering 4d world from monocular video. *arXiv preprint arXiv:2405.18426*, 2024. 2

[56] Zirui Wang, Shangzhe Wu, Weidi Xie, Min Chen, and Victor Adrian Prisacariu. Nerf--: Neural radiance fields without known camera parameters. *arXiv preprint arXiv:2102.07064*, 2021. 3, 7

[57] Guanjun Wu, Taoran Yi, Jiemin Fang, Lingxi Xie, Xiaopeng Zhang, Wei Wei, Wenyu Liu, Qi Tian, and Xinggang Wang. 4d gaussian splatting for real-time dynamic scene rendering. In *Proceedings of the IEEE/CVF Conference on Computer Vision and Pattern Recognition*, pages 20310–20320, 2024. 2, 6, 7, 15, 17, 20, 21

[58] Haolin Xiong, Sairisheek Muttukuru, Rishi Upadhyay, Pradyumna Chari, and Achuta Kadambi. Sparsegs: Real-time 360 {\deg} sparse view synthesis using gaussian splatting. *arXiv preprint arXiv:2312.00206*, 2023. 2, 6

[59] Qiangeng Xu, Zexiang Xu, Julien Philip, Sai Bi, Zhixin Shu, Kalyan Sunkavalli, and Ulrich Neumann. Point-nerf: Point-based neural radiance fields. In *Proceedings of the IEEE/CVF conference on computer vision and pattern recognition*, pages 5438–5448, 2022. 2

[60] Jinyu Yang, Mingqi Gao, Zhe Li, Shang Gao, Fangjing Wang, and Feng Zheng. Track anything: Segment anything meets videos. *arXiv preprint arXiv:2304.11968*, 2023. 2, 3, 4, 6, 7, 10, 11, 12, 13, 19, 20, 21

[61] Lihe Yang, Bingyi Kang, Zilong Huang, Xiaogang Xu, Jiashi Feng, and Hengshuang Zhao. Depth anything: Unleashing the power of large-scale unlabeled data. In *CVPR*, 2024. 2, 4, 6, 10

[62] Ziyi Yang, Xinyu Gao, Wen Zhou, Shaohui Jiao, Yuqing Zhang, and Xiaogang Jin. Deformable 3d gaussians for high-fidelity monocular dynamic scene reconstruction. In *Proceedings of the IEEE/CVF Conference on Computer Vision and Pattern Recognition*, pages 20331–20341, 2024. 6, 7, 15, 17, 20, 21

[63] Zeyu Yang, Hongye Yang, Zijie Pan, and Li Zhang. Real-time photorealistic dynamic scene representation and rendering with 4d gaussian splatting. In *International Conference on Learning Representations (ICLR)*, 2024. 2, 6, 7, 15, 17, 20, 21

[64] Zongxin Ye, Wenyu Li, Sidun Liu, Peng Qiao, and Yong Dou. Absgs: Recovering fine details in 3d gaussian splatting. In *ACM Multimedia 2024*, 2024. 2

[65] Lin Yen-Chen, Pete Florence, Jonathan T Barron, Alberto Rodriguez, Phillip Isola, and Tsung-Yi Lin. inerf: Inverting neural radiance fields for pose estimation. In *2021 IEEE/RSJ International Conference on Intelligent Robots and Systems (IROS)*, pages 1323–1330. IEEE, 2021. 3

[66] Jae Shin Yoon, Kihwan Kim, Orazio Gallo, Hyun Soo Park, and Jan Kautz. Novel view synthesis of dynamic scenes with globally coherent depths from a monocular camera. In *Proceedings of the IEEE/CVF Conference on Computer Vision and Pattern Recognition*, pages 5336–5345, 2020. 6, 10, 12, 13

[67] Jiawei Zhang, Jiahe Li, Xiaohan Yu, Lei Huang, Lin Gu, Jin Zheng, and Xiao Bai. Cor-gs: Sparse-view 3d gaussian splatting via co-regularization. *arXiv preprint arXiv:2405.12110*, 2024. 2

[68] Qiang Zhang, Seung-Hwan Baek, Szymon Rusinkiewicz, and Felix Heide. Differentiable point-based radiance fields for efficient view synthesis. In *SIGGRAPH Asia 2022 Conference Papers*, pages 1–12, 2022. 2

[69] M. Zwicker, H. Pfister, J. van Baar, and M. Gross. Ewa splatting. *IEEE Transactions on Visualization and Computer Graphics*, 8(3):223–238, 2002. 3